

# Journal of Geophysical Research: Space Physics

## RESEARCH ARTICLE

10.1002/2015JA022327

**Key Points:**

- Pitch angle anisotropy of SEP ions at Mars varies with heliospheric conditions
- Variability in MAVEN SEP ion measurements has several different nonheliospheric causes
- Blockage (i.e., shadowing) of energetic ions by Mars is energy dependent and highly variable

**Correspondence to:**R. J. Lillis,  
rlillis@SSL.Berkeley.edu**Citation:**

Lillis, R. J., C. O. Lee, D. Larson, J. G. Luhmann, J. S. Halekas, J. E. P. Connerney, and B. M. Jakosky (2016), Shadowing and anisotropy of solar energetic ions at Mars measured by MAVEN during the March 2015 solar storm, *J. Geophys. Res. Space Physics*, 121, doi:10.1002/2015JA022327.

Received 30 DEC 2015

Accepted 22 MAR 2016

Accepted article online 30 MAR 2016

## Shadowing and anisotropy of solar energetic ions at Mars measured by MAVEN during the March 2015 solar storm

Robert J. Lillis<sup>1</sup>, Christina O. Lee<sup>1</sup>, Davin Larson<sup>1</sup>, Janet G. Luhmann<sup>1</sup>, Jasper S. Halekas<sup>2</sup>, Jack E. P. Connerney<sup>3</sup>, and Bruce M. Jakosky<sup>4</sup>

<sup>1</sup>Space Sciences Laboratory, University of California, Berkeley, California, USA, <sup>2</sup>Department of Physics and Astronomy, University of Iowa, Iowa City, Iowa, USA, <sup>3</sup>Laboratory for Atmospheric and Space Physics, University of Colorado Boulder, Boulder, Colorado, USA, <sup>4</sup>NASA Goddard Space Flight Center, Greenbelt, Maryland, USA

**Abstract** The Solar Energetic Particle (SEP) Instrument on the Mars Atmosphere and Volatile Evolution (MAVEN) spacecraft is meant to characterize the variability of SEP fluxes at Mars. SEP ion precipitation is an important source of heating, ionization, and chemical changes in the upper atmosphere of Mars and may have played a substantial role in driving atmospheric escape over the history of the solar system. Here we examine SEP fluxes during a series of solar disturbances in late February through early March 2015. We present the first SEP ion pitch angle distributions measured at Mars and show how SEP anisotropy changes over the course of the event period. We present examples and explanations of several different kinds of variability in the SEP flux measured in the four fields of view of the instrument. Finally, we present a statistical study of energy- and angle-dependent shadowing of SEP under three different sets of heliospheric conditions, showing that the direct shadowing of SEP by the solid planet may be better explained in terms of simple geometry under quieter heliospheric conditions. In-depth understanding of the effects on SEP fluxes and precipitation patterns by the complex interplay between solar wind disturbances and Mars' magnetospheric configuration awaits detailed modeling studies.

### 1. Introduction

One of the primary goals of the Mars Atmosphere and Volatile Evolution (MAVEN) mission is to characterize the inputs of solar energy into the Martian atmosphere. These include solar extreme ultraviolet radiation, solar wind, and solar energetic particles (SEPs), each of which MAVEN is instrumented to measure [Jakosky *et al.*, 2015a]. SEPs are known to cause heating, ionization, and chemical changes in terrestrial planet atmospheres [e.g., Seppälä *et al.*, 2008; Velinov and Mateev, 1996] and have been observed to cause ionization in the Martian atmosphere, as evidenced by the production of suprathermal secondary electrons [Lillis *et al.*, 2012] and the absorption of radar waves [Espley *et al.*, 2007; Morgan *et al.*, 2006]. These effects have been inferred to cause increases in the escape rate of planetary ions from Mars [Futaana *et al.*, 2008] and are therefore of major interest to the broader problem of Mars climate evolution, as it is thought that SEP events were stronger and/or more frequent in the early solar system [Lillis *et al.*, 2015; Walker, 1975].

The energetic particle environment in near-Mars space has been sampled by a number of instruments, covering different energy ranges and from different orbits. The solar low-energy detector (SLED) instrument on Phobos-2 measured SEPs from 34 keV to 4.5 MeV in five energy channels for 3 months in 1989 in a ~6300 km circular equatorial orbit [McKenna-Lawlor *et al.*, 1992]. Background count rates in the Mars Global Surveyor (MGS) electron reflectometer were used to derive fluxes of 20–100 MeV ions in a ~400 km Sun-synchronous circular polar orbit from 1999 until 2006 [Delory *et al.*, 2012]. The Mars Odyssey Martian Radiation Experiment (MARIE) instrument measured radiation dose at human-relevant energies (i.e., above 30 MeV) from October 2001 to October 2003 [Zeitlin *et al.*, 2004] in a similar orbit to MGS, after which the background rates in the Odyssey High-Energy Neutron Detector and Gamma Ray Spectrometer have been used as proxies until the present for SEP flux above 16 MeV [Zeitlin *et al.*, 2010]. Background count rates in the Mars Express Analyzer of Space Plasmas and Energetic Atoms-3 plasma suite have similarly been used as proxies for SEPs above ~20 MeV in its 300 km × 10,000 km elliptical polar orbit [Frahm *et al.*, 2013; Lillis *et al.*, 2010].

The solid planet Mars forms a barrier to energetic particles. The flux and spectrum of SEPs at a given location in the Martian atmosphere or in near-Mars space are affected by this barrier. Hereafter, we will call the

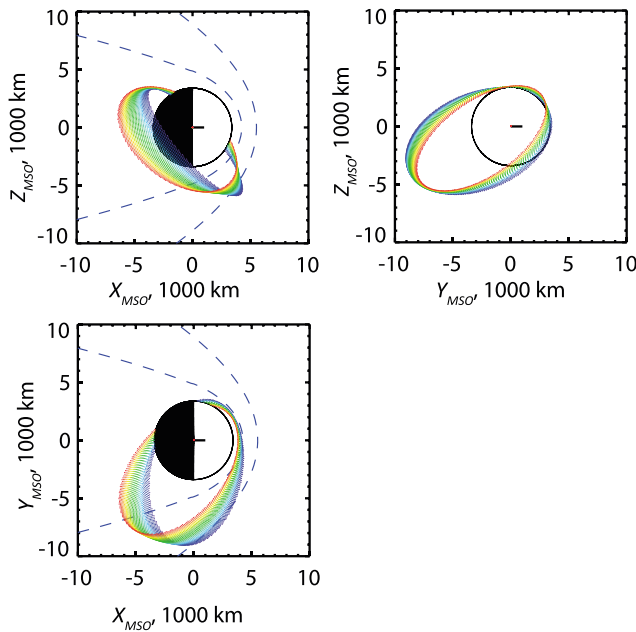


**Figure 1.** Orbital trajectory of MAVEN during the 18 day period of this study, from 25 February 2015 (purple) to 15 March 2015 (red) in the Mars-Solar-Orbital (MSO) coordinate system. The top left shows the perspective from the downside of Mars. The top right shows the perspective looking “down” on the plane of the ecliptic. The bottom left shows the view from the sun. The outer and inner dashed lines are the nominal bow shock and magnetic pileup boundary locations determined by *Trotignon et al. [2006]*.

ments were restricted to a 30° wide cone-shaped instrument field of view (FOV). A modeling-only study by *Leblanc et al. [2002]* considered SEP shadowing but mainly focused on the effects of atmospheric absorption and deflection by magnetospheric and crustal magnetic fields. Lastly, *McKenna-Lawlor et al. [2012]* modeled the motion of energetic ions using a hybrid plasma interaction model and reproduced the approximate shape of the magnetic shadow measured by Phobos-2 SLED.

In this paper we present case studies and statistics of magnetic shadowing of ions from 20 keV to 6 MeV as measured by the MAVEN Solar Energetic Particle Instrument (also referred to by the acronym “SEP”) during a series of heliospheric disturbances in near-Mars space that occurred from 25 February to 15 March 2015, which were triggered by at least four ICMEs (interplanetary coronal mass ejections) [*Jakosky et al., 2015b*]. This is the first time that solar energetic ions have been measured in near-Mars space with high-energy resolution and simultaneous measurements of the IMF, allowing us to examine the complex interplay between SEP, the IMF, and the solid planet.

The second section discusses the data used. The third section examines the broad characteristics of the anisotropy of SEP fluxes during the event period. The fourth section presents specific examples of complex, energy-dependent shadowing of SEP. The fifth section presents statistics of SEP fluxes measured in near-Mars space (and which therefore impacted Mars) during this time. The sixth and final section contains discussion and conclusions.

## 2. Data Used in This Study

The specific SEP data we examine span the time range 25 February 2015 to 15 March 2015 and encompass the entire set of heliospheric disturbances as they impacted Mars. Figure 1 shows the precessing MAVEN orbital trajectory during the event with respect to the nominal magnetic pileup boundary and bow shock locations determined by *Trotignon et al. [2006]*. The MAVEN periapsis pass was on the dayside between 3 PM and 4 PM local time in the northern hemisphere. Also, during this event period MAVEN exited the Mars

resulting decreases in the SEP flux “magnetic shadowing.” The shadowing effect depends upon (1) the energy and pitch angle distribution of SEPs striking the Mars system, (2) the altitude of the observer above the solid planet, and (3) the angular position of the observer with respect to both the planet and the interplanetary magnetic field (IMF) which guides the motion of the SEP. The magnetic shadowing effect of solar particle radiation is important to understand from the perspective of energy deposition in Mars’ upper atmosphere as well as from the human health perspective for human exploration at Mars. Shadowing was first noticed as orbit-period dips in flux measured by SLED and reported on by *Afonin et al. [1989]* though no in-depth analysis or statistics were presented. *Luhmann et al. [2007]* reported on orbital period variability of tens of percent in the omnidirectional flux of 20–200 MeV ions as measured by MARIE; they conducted simple modeling to show that 1 MeV ion fluxes at 400 km altitude could exhibit variability and that fluxes could drop out entirely if measure-

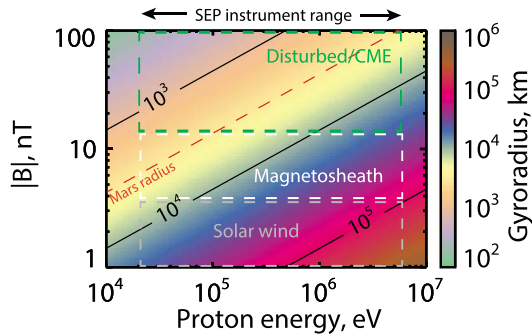


**Figure 2.** Proton gyroradii are plotted with colors as a function of energy and magnetic field strength. The dashed boxes' horizontal extent is the ion energy range of the SEP instrument, while their vertical extent shows approximately the range of magnetic field strengths for different plasma regimes: solar wind (gray), magnetosheath (white), and CME (green). The magnetic pileup region and ionosphere are omitted because SEP collect negligible data in these regions since the attenuators are closed below 500 km during this time period.

large SEP events and do close to protect the detectors when the Sun is in the field of view or when the spacecraft is below 500 km (both sunlight and atomic oxygen can damage the detectors). The interested reader is directed to Larson et al. [2015] for a full description of the instrument design, operation, and data products.

We also use solar wind energy, density and velocity measurements from the Solar Wind Ion Analyzer (SWIA) [Halekas et al., 2015], magnetic field measurements from the MAVEN magnetometer [Connerney et al., 2015], and ancillary data such as the attenuator state, fraction of each FOV blocked by Mars, and spacecraft location and FOV look directions in MSO (Mars-solar-orbital) coordinates.

In addition, for the first time, we use pitch angle distributions (PADs) of energetic ions which we determine in the following manner: (1) resample magnetic field measurements to the cadence of the SEP measurements (2, 8, or 32 s depending on altitude); (2) divide each of the 4 SEP FOVs into  $1^\circ \times 1^\circ$  pixels and calculate the angle of each pixel with respect to the magnetic field, i.e., the pitch angle of the pixel; and (3) divide pitch angle space ( $0^\circ$ – $180^\circ$ ) into  $10^\circ$  bins and assign to each  $10^\circ$  bin the mean flux of any FOV whereby the pitch angles overlap that bin, weighted by the size of the overlap. With most pitch angle bins having zero, one, or two FOVs contributing, formal PAD errors are difficult to quantify but can be approximated by the scatter between adjacent pitch angle bins. PADs are meaningful only when the first adiabatic invariant is conserved; i.e., the radius of magnetic field curvature is much larger than the ion gyroradius [e.g., Parks, 2004]. Despite the existence of relatively small-scale features such as turbulence and magnetic holes which can alter the particles' paths on scales smaller than their gyroradii, this is mostly true in the solar wind where the field line curvature of the interplanetary magnetic field is typically on the order of millions of kilometers. However, it is not necessarily true inside the Martian magnetosphere where the field line curvature can be on the order of the planetary radius or smaller. These energetic ions measured by the SEP instrument have gyroradii of tens to hundreds of thousands of kilometers (see Figure 2), and therefore, we calculate PADs with respect to the nearest measurement of the IMF made outside the Martian bowshock.

### 3. Large-Scale Character and Anisotropy of the Multi-ICME Event Period

Before examining specific signatures or statistics of SEP shadowing during our event period, it helps to first examine the large-scale features, particularly those that concern SEPs. Figure 3 shows a time series of the energetic ion fluxes in one forward and one reverse look directions (i.e., 1 F and 1 R), ion PADs at 100 keV and 500 keV, IMF direction and strength, and solar wind pressure together with the energy-pitch angle spectrograms of SEPs measured outside the bow shock. Correlated with the increases in the SEP flux distributions, the time series show a series of prompt increases in the IMF strength and solar wind pressure, indicating the shock arrival of four ICMEs at Mars. Note that although the third shock is very weak in terms of the peak solar

magnetosphere into the upstream solar wind for almost 2 h on each orbit, which allowed for measurements of the IMF, i.e., the large-scale magnetic structures that primarily govern SEP ion motion, as was described by Jakosky et al. [2015b]

The SEP instrument data used in this study are in the form of ion differential energy fluxes in 28 logarithmically spaced energy bins spanning 20 keV to 6 MeV (see Figure 8 of Larson et al. [2015] for the energy map) in four orthogonal look directions lying in a plane at  $90^\circ$  angles to each other, each with a total field of view of  $42^\circ \times 31^\circ$  ( $\sim 3\%$  of the full sky). These are labeled 1 F, 1 R, 2 F, and 2 R, where the numbers denote the SEP instrument sensors and "F" and "R" denote the "forward" FOV (usually oriented  $45^\circ$  away from the Mars-Sun line) and "reverse" FOV (usually oriented  $135^\circ$  away from the Mars-Sun line). SEP have attenuators which, when closed, reduce the count rate by a factor of  $\sim 100$ . The attenuators can close to increase the dynamic range during very

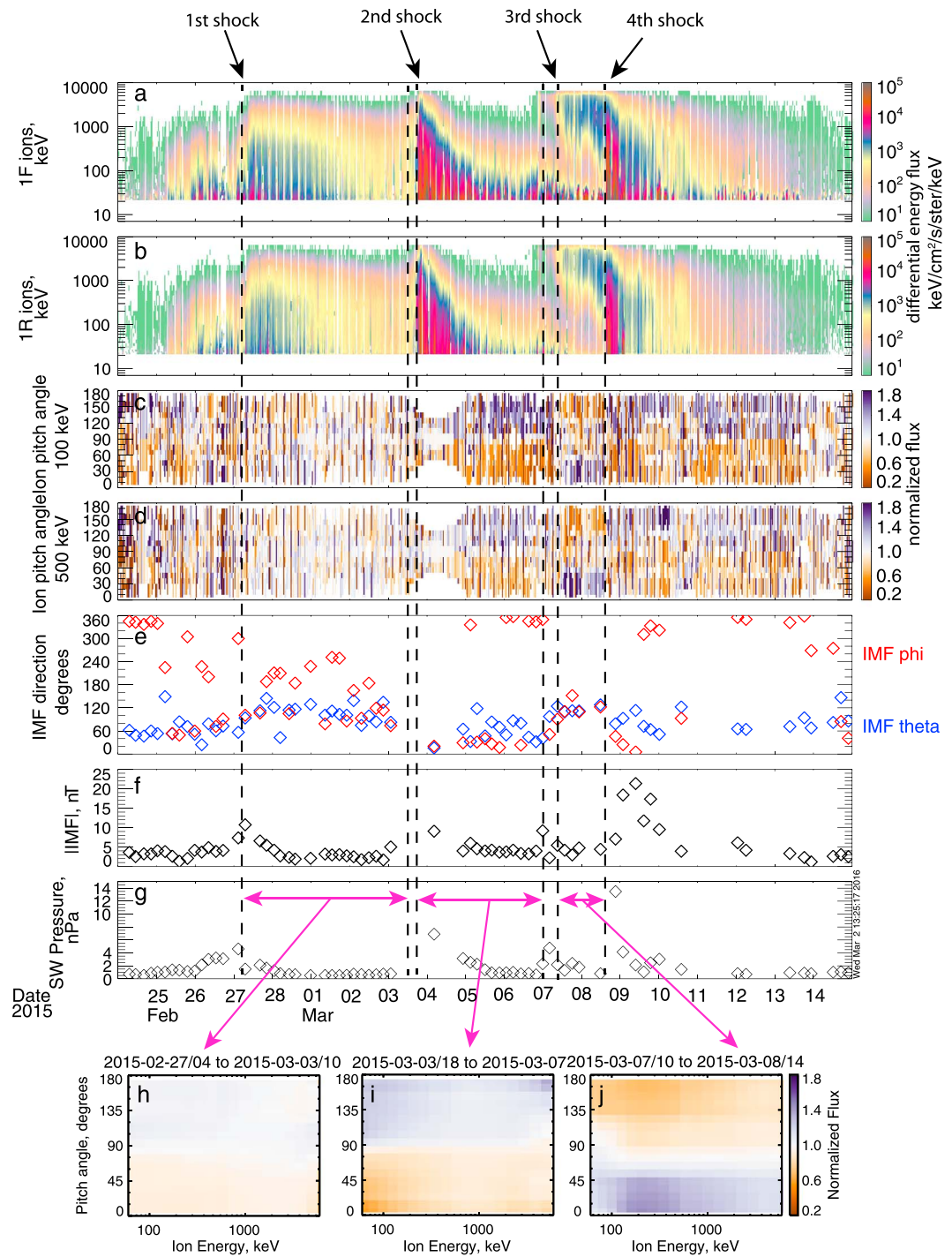


**Figure 3.** Overview of the February–March 2015 series of solar disturbances measured at Mars. The panels are as follows from top to bottom: (a, b) energetic ion differential energy fluxes ( $\text{keV}/\text{cm}^2/\text{s}/\text{sr}/\text{keV}$ ) in the two forward look directions (each pointed  $\sim 45^\circ$  away from the Sun during most of each orbit), (c, d) ion pitch angle distributions at 100 keV and 500 keV, (e) interplanetary magnetic field (IMF) direction in the Mars-Solar-Orbital (MSO) coordinate system where the blue and red diamonds represent the polar and azimuth angles respectively, (f, g) IMF strength (nT) and solar wind pressure. The latter three are measured outside the bow shock during most orbits over this time range. (h, i, and j) Energy-pitch angle spectrograms of SEP ions measured in the solar wind, averaged over three distinct time periods denoted by pink horizontal arrows in Figure 3g. Energies below 60 keV are omitted from these spectrograms because these energies are often contaminated by signals from non-SEP pickup oxygen ions [Rahmati et al., 2015].

wind pressure and IMF values, the flux spectra show an early onset of the highest-energy SEPs (with peak fluxes possibly above the SEP instrument upper energy limit of 6 MeV) prior to the arrival of the fourth ICME shock. These high-energy SEP arrived about 2 days prior to the lower energy SEPs, indicating that these SEP were accelerated near the Sun during the early phase of the fourth ICME event [Jakosky *et al.*, 2015b].

In addition to those aspects, we report here the first measurements of pitch angle anisotropy of SEPs striking Mars. First, we see a correlation between IMF direction and pitch angle anisotropy. During this time, the polar angle (theta) component of the IMF in the MSO coordinate system is largely between  $60^\circ$  and  $120^\circ$ , i.e., within  $30^\circ$  of the ecliptic plane. For several days following the first shock, the SEPs are quite isotropic over all energies, as the azimuthal (phi) component of the IMF varies between  $\sim 90^\circ$  and  $240^\circ$ . Following the second shock, the SEP distribution becomes anisotropic as the IMF oscillates close to an azimuth of  $0^\circ/360^\circ$ , i.e., pointing close to the Mars-Sun line. As expected, during this time the SEP flux distribution at all measured energies is approximately three times higher antiparallel to the magnetic field than parallel; i.e., more SEPs are traveling in the  $-x$  direction (away from the Sun) than the  $+x$  direction (toward the Sun). However, this still indicates that a nonnegligible source of SEPs is connected to Mars via a magnetic field line that extends beyond Mars' orbit from the Sun. When the third (weak) shock and storm of high-energy particles reaches Mars on 7 March, the IMF turns and its phi angle is  $\sim 120^\circ$ , i.e., a typical Parker spiral, for about 30 h. The SEPs are now more parallel than antiparallel, traveling in the  $-x, +y$  direction, i.e., more away from the Sun as expected. Following the fourth shock, the same pattern continues for several days, with a preference for an antiparallel particle distribution when the IMF is approximately sunward and parallel distribution when the IMF briefly has a Parker spiral configuration, such as on 10 March. The bottom three panels in Figure 3 show that SEP pitch angle anisotropy is not strongly energy dependent, being somewhat more pronounced at the lowest and highest energy during interval 2 and in the range 100–300 keV during interval 3.

#### 4. Interpreting Flux Variations in SEP Ion Data

Energetic ion fluxes entering the four fixed SEP FOVs are dependent on three main factors. The first factor is the energy and angular distribution of energetic ions striking the Mars system, which is responsible for the long-term features of the SEP flux such as those shown in Figure 3. These distributions depend on heliospheric conditions such as flares (which accelerate SEPs at the Sun), CME shocks (which accelerate SEPs locally), and the solar wind and IMF configuration which guides the accelerated particles toward or away from Mars. The second factor is the spacecraft location within or with respect to the Martian magnetosphere, since the draped IMF above 500 km (i.e., where useful SEP data exist) can be up to tens of nT [Brain *et al.*, 2003] and can deflect some of the lower energy SEPs ( $<300$  keV). See Figure 2 for the gyroradii of solar energetic protons as a function of magnetic field strength and energy.

The third factor is the spacecraft attitude, which changes typically on a two-orbit cadence as maneuvers are executed for different observations near periapsis, on the flanks of the orbit, and near apoapsis. The spacecraft attitude also changes for less common activities such as reaction wheel desaturations and Earth communication [Jakosky *et al.*, 2015a]. Attitude changes expose each FOV to a different part of the local SEP angular distribution, which can itself be heavily influenced by proximity to the solid planet and (to a lesser degree) by its atmosphere, which can block, in an energy-dependent way, some SEP from entering a given FOV.

Figure 4 shows examples of the second and third factors. Spanning  $\sim 14$  h in 2 March to 3 March, the heliospheric source of SEPs does not change substantially (see Figure 3). Therefore, most of the energy-dependent variability in ion fluxes entering the four FOVs is due to their orientation with respect to the local angular distribution of energetic ions, both of which change as the spacecraft orbits Mars (as shown in Figure 1), spending  $\sim 2$  h per orbit in the solar wind.

Six types of flux variations are shown in this example, each with a different explanation, and summarized in Table 1. The first is caused by the attenuators closing near each periapsis. Figures 4a–4e show that even though the calculated fluxes are adjusted for the much smaller ( $x \sim 100$ ) geometric factor when the attenuators are closed, so few counts are recorded that reliable fluxes cannot be derived.

The second type is caused by the solid planet obstructing the 2R field of view, at times labeled "A1" and "A2," on the inbound leg of the orbit  $\sim 1000$  km altitude around local noon in the southern hemisphere. Using simple geometry we can roughly estimate the range of ion energies that should be blocked by Mars. This range

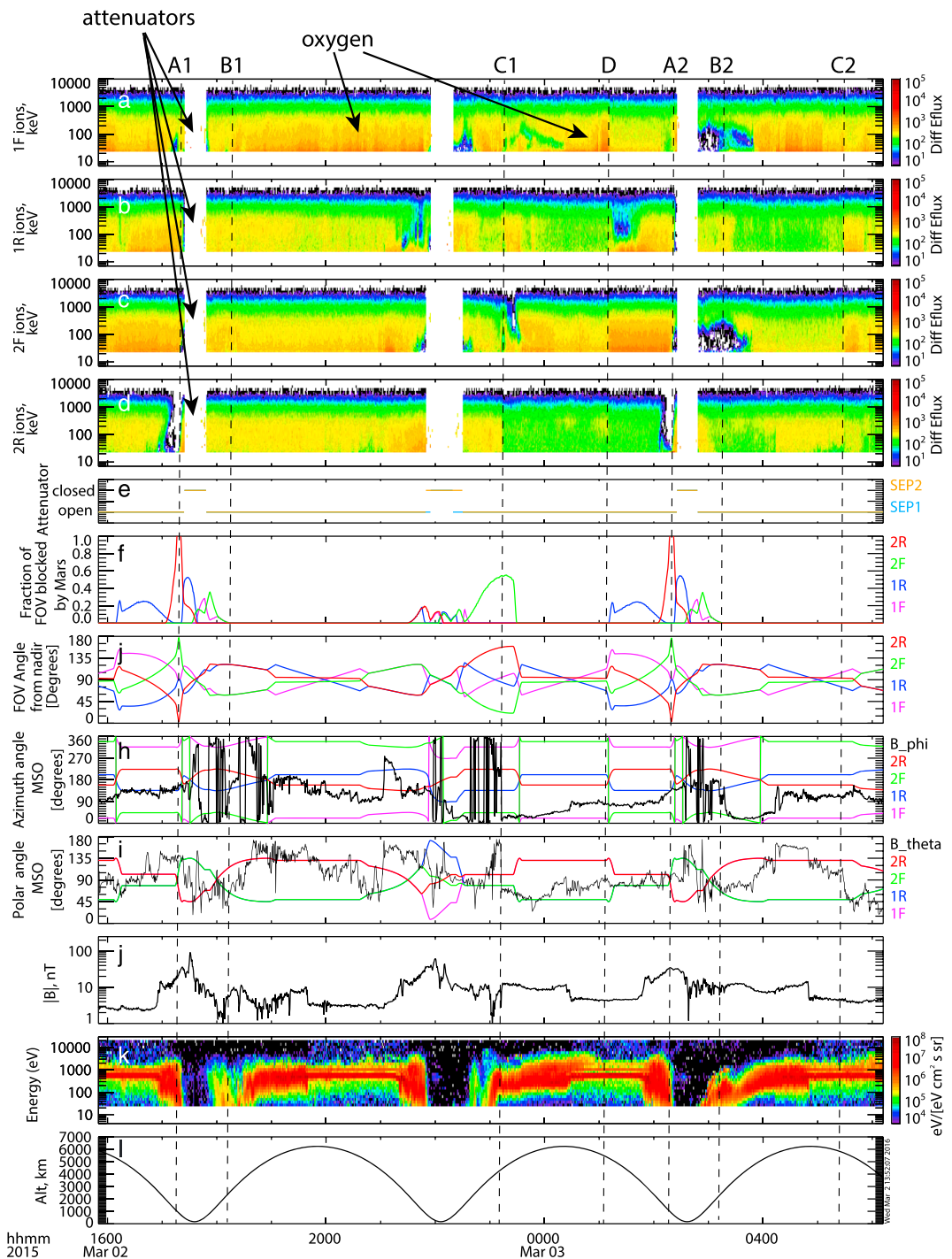


**Figure 4.** Time series demonstrating the different nonheliospheric sources of variability in the energetic ion flux measured by the SEP instrument. From top to bottom, (a–d) energy-time spectrograms of ion differential energy flux in the four SEP FOVs, (e) the attenuator state of both SEP sensors 1 and 2, (f, g) fraction of each FOV which sees the solid planet and the angle of the center of each FOV with respect to the center of Mars, (h, i) the MSO azimuthal ( $\phi$ ) and polar ( $\theta$ ) angles of each of the FOVs and the magnetic field, (j) the magnetic field magnitude, (k) omnidirectional ion energy-time spectrograms from the SWIA instrument, and (l) the altitude of the spacecraft. The vertical dashed lines refer to specific events discussed in the text and summarized in Table 1.

**Table 1.** Ion Flux Variations Measured by SEP and Their Causes, Excluding Natural Heliospheric Variability<sup>a</sup>

Labels	Event Type	Description and Explanation
"Attenuators"	Attenuators closing	Attenuators close to protect detectors from sunlight and atomic oxygen, reducing geometric factor by ~100. This results in too few counts to derive reliable fluxes.
A1, A2	Higher-energy shadowing	Dropouts in high- and medium-energy ion fluxes in 2R because Mars completely obstructs FOV ~20 min before periapsis. Therefore, larger gyroradii particles are shadowed by Mars.
B1, B2	Low-energy shadowing	Dropouts and lower energy ion fluxes outbound in magnetosheath because low-energy SEP with $R_{\text{gyro}} < \sim R_{\text{Mars}}$ are shadowed by Mars at time B2 but not B1 due to different magnetosphere conditions.
C1, C2	Magnetic field rotation	At high altitudes, fixed FOVs see sharp ion flux variation below ~400 keV as ion angular distribution changes in response to rapid change in magnetic field direction. Higher-energy ion fluxes vary much less due to being less sensitive to local magnetic field changes.
D	Spacecraft reorientation	In the solar wind, sharp ion flux variation below ~400 keV due to FOVs moving to sample different part of a fairly constant ion angular distribution. Higher-energy ion fluxes vary much less due to being more isotropic.
"Oxygen"	Pickup oxygen ions	Bursty, highly directional fluxes at detected energies below 100 keV caused by newly ionized oxygen atoms accelerated by the solar wind convection electric field

<sup>a</sup>The left column refers to the labels at the top of Figure 4.

varies with the angle between the magnetic field and a plane tangential to the planet, with more radial magnetic field directions resulting in a larger range of blocked energies. Figure 5 shows one useful case of this geometry where the field is parallel to this tangent plane (and applies for any azimuthal direction about a normal to this plane). The geometry shown is both relevant for data collected near periapsis during this time (i.e., where the draped IMF is typically tangential to the surface) and also lets us derive, using the law of cosines, the maximum energy  $E_{\max}$  of an ion that can reach a detector at altitude  $h$  with a velocity that makes an angle  $\alpha$  to the nadir direction (as given by equation (1)). All energies higher than this should be blocked by the solid planet, regardless of the magnetic field direction. Figure 5 also shows this geometry.

$$E_{\max} = \frac{B^2 R_g^2 q^2}{2m}, \quad R_g = \frac{h^2 + 2hR_M}{2[R_M(1 - \sin\alpha) - h\sin\alpha]} \quad (1)$$

where  $B$  is the assumed uniform magnetic field strength,  $R_g$  is the ion gyroradius,  $m$  and  $q$  are the mass and charge of the ion, and  $R_M$  is the radius of Mars, all in SI units.

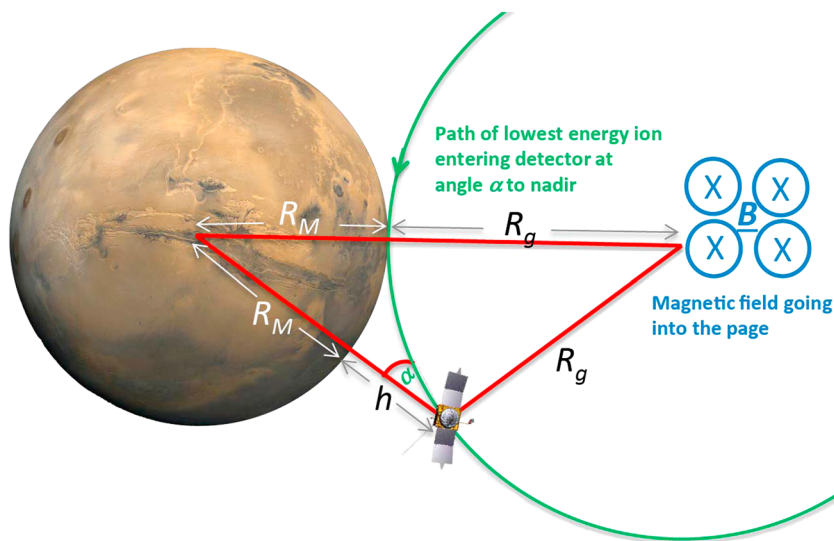


**Figure 5.** Illustration depicting high-energy shadowing of energetic ions in an idealized situation of a uniform magnetic field. The green path represents the trajectory of the highest-energy ion that can enter the detector at an angle  $\alpha$  to nadir if the spacecraft is at altitude  $h$ . Equation (1) relates the angle between nadir and ion velocity at the spacecraft to spacecraft altitude and ion gyroradius.

If the 2R aperture, at 1000 km altitude, points at the center of Mars, then all ions with gyroradii above ~1600 km will be blocked by Mars from entering the aperture. If we make the simplifying assumption that the measured magnetic field of 15 and 22 nT guides the particles' trajectory everywhere and that protons dominate the SEP population, then the particles above ~30 keV and ~60 keV will not be able to enter the 2R aperture, respectively. This is indeed the observed behavior during the flux dropouts at times A1 and A2, respectively in Figure 4d). We label these events "high-energy shadowing" events because the solid planet forms a shadow for all SEPs above a certain cutoff energy, which is determined by the spacecraft altitude and the magnetic field strength.

In contrast, the third type of flux variation is characterized by dropouts at an intermediate range of energies, which we call "low-energy shadowing." These are related to the high-energy shadowing events in that the decreased fluxes are caused by the solid planet obstructing ions. However, in this case the FOV is typically not facing the planet (see Figure 4g), so the highest-energy ions with the largest gyroradii are not obstructed. At any given time, the energy range of ions that are shadowed and the depth of the decrease is dependent on the angular distance between the FOV and the solid planet, as well as the angular distribution of ions as they gyrate in the Martian magnetosphere. Because the heliospheric source of the SEPs was mostly constant for this time period, if the Martian magnetosphere was stable from time B1 to time B2 in Figure 4, we should see very similar dropouts at these times because the spacecraft position (1000–3000 km altitude near local midnight in the northern hemisphere) and attitude with respect to Mars and the Sun was identical. However, we see a ~60 min dropout in FOVs 1 F and 2 F (Figures 4a and 4c) at time B2 but no dropout at B1 because the magnetosphere was quite different: at B1 the magnetic field was highly variable though largely sunward and quite weak (see Figures 4h–4j), falling as low as 1 nT with some hot sheath-like plasma present in the SWIA data (Figure 4k), whereas at B2 the field was largely antisunward with a strength of ~10 nT and a more typical tail-like ion spectrum measured by SWIA. Detailed modeling of both the magnetosphere and SEP particle traces is required to understand the exact shape of these dropouts and is beyond the scope of this paper.

The fourth type of flux variation occurs when MAVEN encounters a very different magnetic field environment, resulting in a sudden change in the angular distribution of the SEPs at a time when the FOVs look directions are not varying. The change is always more acute for lower energies since their paths are more strongly affected by the changing magnetic environments. Examples of this are shown at times C1 and C2 in Figure 4, with the former being clearer. During the time C1, at ~4000 km altitude in the tail lobe, the magnetic field strength increases by ~20% (Figure 4j) and its direction changes abruptly from northward-antisunward to ecliptic-sunward (Figures 4h and 4i), with a resultant change in the fluxes in all four FOVs (a high-energy shadowing event in 2 F complicates the picture somewhat). The clearest signature is shown for 2R (Figure 4d), with a decrease by almost an order of magnitude. C2 occurs in the solar wind with a rapid change from a typical ecliptic Parker spiral direction to a more southward magnetic field configuration, resulting in modest increases in the fluxes in 1R and 2F but no obvious changes in the other FOVs.

The fifth type of SEP flux variation occurs when the magnetic field is constant but the spacecraft reorients, such as at time D. Here the spacecraft is in a stable IMF of about 4 nT with a positive  $B_z$ , when the spacecraft reorients moderately, exposing the FOVs to different portions of the ion angular distributions. This results in noticeably lower fluxes in 1 F, higher fluxes in 2 F, no change in 2R, and a medium-energy shadowing event in 1R.

The sixth and final type of flux variation observed in SEP ion data is caused by ionized exospheric oxygen picked up by the solar wind and accelerated to energies from a few tens of keV up to 200 keV. Because they lose significant energy in the aluminum and silicon dead layer coating the "open" detectors [Larson et al., 2015], they are detected at energies typically below 100 keV. They travel in cycloidal paths in the antisunward direction and so are only observed in the 1 F and 2 F (i.e. typically sunward facing) FOVs. In Figure 4a they can be seen as bursty features at low energies superimposed on the solar energetic proton flux at most times except between times D and A2 and when extinguished by either type of shadowing. The source and character of these pickup oxygen ions is discussed in detail by Rahmati et al. [2015].

## 5. Statistical Properties of SEP Shadowing

We know from time series of energetic ion flux (like that shown in Figure 4) that shadowing of SEPs by the solid planet occurs regularly. Therefore, we examine the statistics regarding how this shadowing varies with energy, altitude, the angle of the FOV center with respect to Mars, and heliospheric conditions. It is not useful

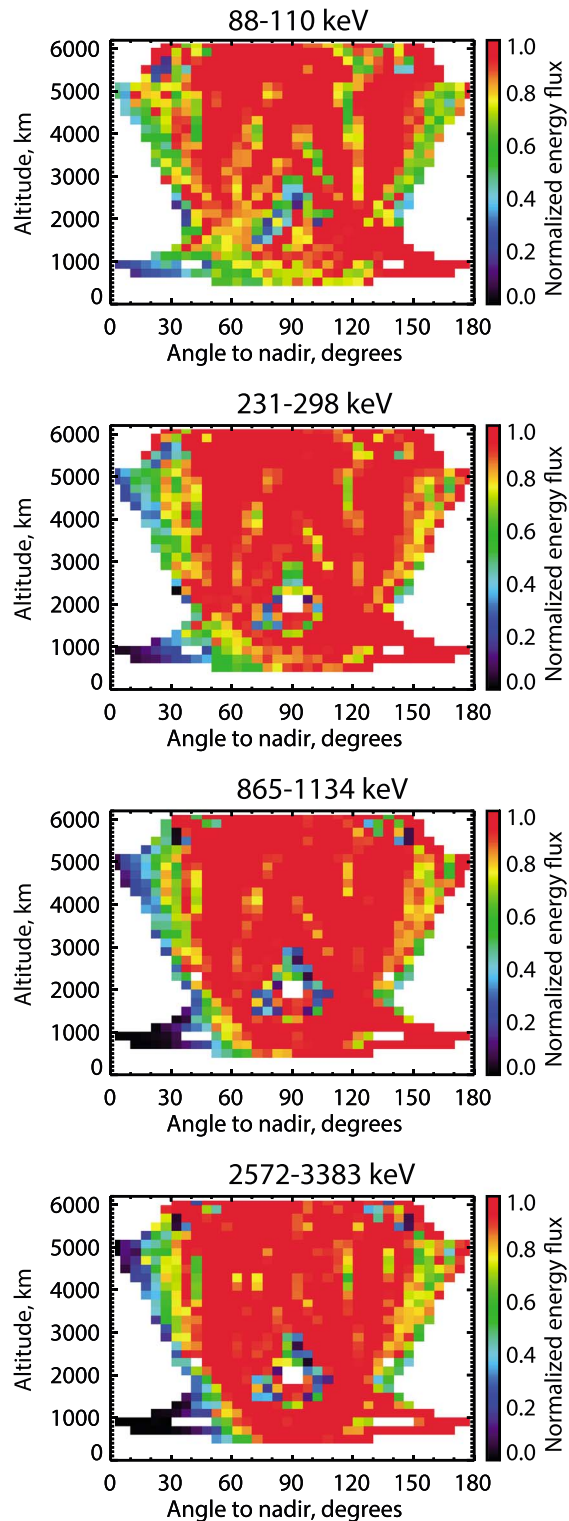


**Figure 6.** Colors represent differential ion energy flux from all four SEP FOVs over the entire period from 25 February 2015 to 15 March 2015, normalized by the nearest-in-time average flux measured above 5000 km and averaged over bins of  $5^\circ$  in nadir angle (i.e., the angle between the FOV boresight and the center of the planet) and 200 km in altitude, in four representative energy ranges: 88–110 keV, 231–298 keV, 865–1134 keV, and 2572–3383 keV.

to compare or average together absolute differential energy fluxes from different parts of this event because they vary over more than 5 orders of magnitude in time and energy. Therefore, we calculate a “normalized ion energy flux” by dividing the differential energy flux in each energy bin by the mean of all the fluxes measured above 5000 km altitude at the nearest apoapsis in time. By doing this, we hope to isolate the shadowing effects of the solid planet. Figures 6 shows this normalized energy flux over the whole event, for all four FOVs, averaged in bins of  $5^\circ$  in nadir angle and 200 km in altitude, for four representative energy channels. The  $0^\circ$  nadir angle means that the FOV boresight is in the direction of the center of the planet, i.e., radially downward, and  $180^\circ$  is radially upward.

Although the sampling determined by the orbit and attitude of the MAVEN spacecraft is somewhat limiting, the pattern shown is consistent with discussions in the previous section: ion fluxes decrease as nadir angles and altitudes decrease, which makes intuitive sense: as more of the sky is blocked by the planet, fewer interplanetary SEPs can enter the detector. As also expected, this effect is more pronounced for higher energies because their larger gyroradii mean that the solid planet blocks their paths into the FOV more effectively; i.e. this is the high-energy shadowing phenomenon discussed in the previous section.

Figure 7 examines how the energy and nadir angle-dependent character of the shadowing changes with the different heliospheric conditions present in intervals 1, 2, and 3 identified (see Figure 3) for all data collected between 500 km and 1000 km altitude, i.e., close to the planet and therefore relevant for understanding SEP precipitation. The white lines represent the maximum calculated energy (according to equation (1)) for which protons can enter the SEP detector at 750 km altitude (i.e., the mean altitude of the spacecraft at which the displayed data were collected), under the simplistic assumption of a uniform magnetic field with a strength equal to the average of the magnetic field measured below 1000 km.

Table 2 shows the mean, median, and standard deviation of magnetic fields measured at the spacecraft below 1000 km during each of the three intervals identified in Figure 3.

The first feature we notice is that the high-energy shadowing phenomenon, most prominent for

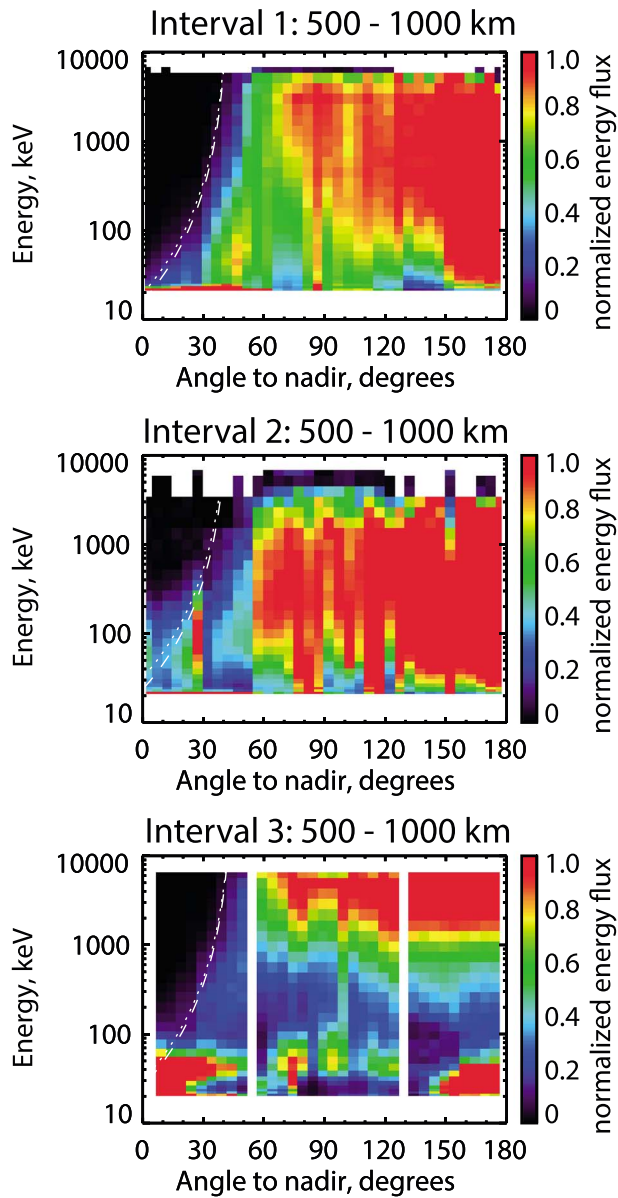


**Figure 7.** Colors represent normalized differential ion energy fluxes from all four FOVs, normalized by the nearest-in-time average flux measured above 5000 km and averaged over bins of  $5^\circ$  in nadir angle and all 28 instrumental energy bins. The top, middle, and bottom are averaged over the three time intervals shown in Figure 3 and for altitudes between 500 and 1000 km. The white curves signify the maximum energy particle which, originating outside the atmosphere, should be able to enter the SEP instrument FOV at 750 km (the mean spacecraft altitude) assuming an ambient magnetic field strength equal to the mean (dotted) and median (dashed) magnetic field measured below 1000 km altitude. The mean and median magnetic field strengths are given in Table 2: 23.0 and 20.7 nT for interval 1, 29.5 and 25.4 nT for interval 2, and 35.0 and 27.8 nT for interval 3, respectively.

higher-energy SEPs entering the detector cannot have passed near the planet and therefore cannot be shadowed. Once again, interval 2 defies easy explanation, where we see an enhancement at middle energies between  $\sim 80$  keV and  $\sim 2$  MeV but essentially no shadowing for nadir angles above  $\sim 120^\circ$ . This is probably due to complex interactions between the ICME shock, the draped magnetosphere, and the incident SEPs.

higher energies and lower nadir angles, is clear in all three intervals. However, it manifests differently each time. For interval 1, when the incident SEPs are fairly isotropic and no shocks occur; our simplistic model is consistent with the data and reproduces the high-energy shadowing reasonably well. For interval 2, during which SEPs travel preferentially away from the Sun approximately along the Mars-Sun line and which includes a time-decaying SEP spectrum following the major CME shock of 3 March, our simplistic model is consistent with the data above  $\sim 500$  keV, below which ions partially “fill in” some of the expected shadow. This filling in could be due to locally much stronger magnetic fields and local particle acceleration as the shock passes through the Martian system. For the short third interval, when no shock occurs and high-energy SEPs dominate and SEPs of all energies preferentially travel away from the Sun along a canonical Parker spiral, our simplistic model is consistent with the data above  $\sim 100$  keV, below which we see some filling in of loss cone, though substantially less than interval 2. The low-energy (20–60 keV) peak at low nadir angles is likely due to occasional magnetic field values much higher than the mean (see Table 2) with some possible contribution from pickup oxygen backscattering from the atmosphere.

The second feature we notice in Figure 7 is the low-energy shadowing phenomenon, i.e., typically lower energy SEPs blocked by the planet at much higher nadir angles, resulting from certain combinations of SEP angle distribution and magnetic field geometry. As we would expect, this also manifests itself differently in each of the three intervals due to different average magnetospheric conditions. Once again, interval 1 is the most regular due to its isotropic SEP angular distribution, no shocks, and broad range of IMF angles, displaying low-energy shadowing for decreasing energies as nadir angles increase beyond  $\sim 60^\circ$ . This makes sense because as the detector aperture points further in angle away from nadir,

**Table 2.** Magnetic Fields Measured at the Spacecraft Altitude Below 1000 km During Each of the Three Intervals Identified in Figure 3

$ B $ , nT Below 1000 km	Interval 1	Interval 2	Interval 3
Mean	23.0	29.5	35.0
Median	20.7	25.4	27.8
Standard deviation	14.3	19.1	23.1

For interval 3, the higher SEP anisotropy and Parker spiral IMF result in 60–90% flux decreases at middle energies near the spacecraft periapsis for all nadir angles, though like in interval 1, the shadowed energies are lower for larger nadir angles.

## 6. Conclusions

In this study we have presented data from the MAVEN SEP instrument collected during the ~18 day series of solar disturbances in March 2015 and attempted to explain, to first order, the variability in observed flux. We have presented the first SEP ion pitch angle distributions measured at Mars and shown that SEPs impacting the Mars system in the first phase of the event were isotropic, whereas those following the 3 March shock were more anisotropic, being enhanced (as expected) in the antisunward direction. We have also shown that the flux measured in any one field of view within and between individual orbits depends on several factors: the instrument attenuators, the flux impacting the Martian system, the local magnetic field configuration, the spacecraft attitude and energy-dependent blockage of energetic ion flux by the solid planet, which we call “shadowing.” Lastly, we have statistically examined shadowing under three different sets of heliospheric conditions and shown that a simple geometric model explains the direct shadowing of high-energy particles ( $>500$  keV) under most conditions but that lower energy shadowing is more complex and depends on the interplay of SEP angular distributions and magnetic field geometry and observation location.

In future work, we intend to further explore the geometry that controls SEP shadowing by examining more SEP events observed by MAVEN. We also intend to conduct test particle modeling to attempt to reproduce observations and thereby understand the effect of SEP shadowing and anisotropy on patterns of solar energetic particle precipitation into the Martian upper atmosphere and their dependencies on heliospheric conditions. Determining how these conditions affect the upper atmosphere of Mars through energetic particle precipitation is an important factor in understanding the complex relationship between solar inputs and atmospheric escape from Mars.

## Acknowledgments

The data used in this study can be accessed through the Planetary Data System Planetary Plasma Interactions node. A special thanks to the engineers and support staff at the UC Berkeley Space Sciences Laboratory who aided D. Larson and R. Lillis in designing, building, testing, and operating the Solar Energetic Particle instrument, including Ken Hatch, Patrick Dunn, Miles Robinson, Chris Tiu, and David Curtis.

## References

- Afonin, V., et al. (1989), Energetic ions in the close environment of mars and particle shadowing by the planet, *Nature*, 341(6243), 616–618.
- Brain, D. A., F. Bagenal, M. H. Acuña, and J. E. P. Connerney (2003), Martian magnetic morphology: Contributions from the solar wind and crust, *J. Geophys. Res.*, 108(A12), 1424, doi:10.1029/2002JA009482.
- Connerney, J. E. P., J. Espley, P. Lawton, S. Murphy, J. Odom, R. Oliversen, and D. Sheppard (2015), The MAVEN magnetic field investigation, *Space Sci. Rev.*, 1–35, doi:10.1007/s11214-015-0169-4.
- Delory, G. T., J. G. Luhmann, D. Brain, R. J. Lillis, D. L. Mitchell, R. A. Mewaldt, and T. V. Falkenberg (2012), Energetic particles detected by the electron reflectometer instrument on the Mars Global Surveyor, 1999–2006, *Space Weather Int. J. Res. Appl.*, 10, doi:10.1029/2012SW000781.
- Espley, J. R., W. M. Farrell, D. A. Brain, D. D. Morgan, B. Cantor, J. J. Plaut, M. H. Acuña, and G. Picardi (2007), Absorption of MARSIS radar signals: Solar energetic particles and the daytime ionosphere, *Geophys. Res. Lett.*, 34, L09101, doi:10.1029/2006GL028829.
- Frahm, R. A., J. R. Sharber, J. D. Wingham, H. A. Elliott, T. A. Howard, C. E. DeForest, D. Odstrčil, E. Kallio, S. McKenna-Lawlor, and S. Barabash (2013), Solar energetic particle arrival at Mars due to the 27 January 2012 solar storm, *AIP Conf. Proc.*, 1539(1), 394–397.
- Futaana, Y., et al. (2008), Mars Express and Venus Express multi-point observations of geoeffective solar flare events in December 2006, *Planet. Space Sci.*, 56(6), 873–880.
- Halekas, J. S., E. R. Taylor, G. Dalton, G. Johnson, D. W. Curtis, J. P. McFadden, D. L. Mitchell, R. P. Lin, and B. M. Jakosky (2015), The MAVEN Solar Wind Ion Analyzer, *Space Sci. Rev.*, 195(1), 125–151.
- Jakosky, B. M., et al. (2015a), The Mars Atmosphere and Volatile Evolution (MAVEN) mission, *Space Sci. Rev.*, 1–46, doi:10.1007/s11214-015-0139-x.
- Jakosky, B. M., et al. (2015b), MAVEN observations of the response of Mars to an interplanetary coronal mass ejection, *Science*, 350(6261), doi:10.1126/science.aad0210.
- Larson, D., et al. (2015), The MAVEN solar energetic particle investigation, *Space Sci. Rev.*, 175, 153–172.
- Leblanc, F., J. Luhmann, R. E. Johnson, and E. Chassefiere (2002), Some expected impacts of a solar energetic particle event at Mars, *J. Geophys. Res.*, 107(A5), 1058, doi:10.1029/2001JA00178.
- Lillis, R. J., D. A. Brain, S. L. England, P. Withers, M. O. Fillingim, and A. Safaeinili (2010), Total electron content in the Mars ionosphere: Temporal studies and dependence on solar EUV flux, *J. Geophys. Res.*, 115, A11314, doi:10.1029/2010JA015698.

- Lillis, R. J., D. A. Brain, G. T. Delory, D. L. Mitchell, J. G. Luhmann, and R. P. Lin (2012), Evidence for superthermal secondary electrons produced by SEP ionization in the Martian atmosphere, *J. Geophys. Res.*, 117, E03004, doi:10.1029/2011JE003932.
- Lillis, R. J., D. A. Brain, S. W. Bouger, F. Leblanc, J. G. Luhmann, and B. Jakosky (2015), Characterizing atmospheric escape from Mars today and through time, with MAVEN, *Space Sci. Rev.*, 195, 357–422.
- Luhmann, J. G., C. Zeitlin, R. Turner, D. A. Brain, G. Delory, J. G. Lyon, and W. Boynton (2007), Solar energetic particles in near-Mars space, *J. Geophys. Res.*, 112, E10001, doi:10.1029/2006JE002886.
- McKenna-Lawlor, S., et al. (1992), Energetic particle studies at Mars by SLED on Phobos-2, *Recent Results Mars Venus*, 12, 231–241.
- McKenna-Lawlor, S., E. Kallio, R. Jarvinen, and V. Afonin (2012), Magnetic shadowing of high-energy ions at Mars and how this effect can be simulated using a hybrid model, *Earth Planets Space*, 64(2), 247–256.
- Morgan, D. D., D. A. Gurnett, D. L. Kirchner, R. L. Huff, D. A. Brain, W. V. Boynton, M. H. Acuña, J. J. Plaut, and G. Picardi (2006), Solar control of radar wave absorption by the Martian ionosphere, *Geophys. Res. Lett.*, 33, L13202, doi:10.1029/2006GL026637.
- Parks, G. K. (2004), *Physics of Space Plasmas*, 597 pp., Westview Press, Oxford.
- Rahmati, A., D. E. Larson, T. E. Cravens, R. J. Lillis, P. A. Dunn, J. S. Halekas, J. E. Connerney, F. G. Eparvier, E. M. B. Thiemann, and B. M. Jakosky (2015), MAVEN insights into oxygen pickup ions at Mars, *Geophys. Res. Lett.*, 42, 8870–8876, doi:10.1002/2015GL065262.
- Seppälä, A., M. A. Clilverd, C. J. Rodger, P. T. Veronen, and E. Turunen (2008), The effects of hard-spectra solar proton events on the middle atmosphere, *J. Geophys. Res.*, 113, A11311, doi:10.1029/2008JA013517.
- Trotignon, J. G., C. Mazelle, C. Bertucci, and M. H. Acuna (2006), Martian shock and magnetic pile-up boundary positions and shapes determined from the Phobos 2 and Mars Global Surveyor data sets, *Planet. Space Sci.*, 54(4), 357–369.
- Velinov, P. I., and L. Mateev (1996), An improved model for the influence of cosmic rays and high-energy particles on the ionosphere and middle atmosphere, *Adv. Space Res.*, 18(3), 23–27.
- Walker, R. M. (1975), Interaction of energetic nuclear particles in space with the lunar surface, *Annu. Rev. Earth Planet. Sci.*, 3, 99–128.
- Zeitlin, C., T. Cleghorn, F. Cucinotta, P. Saganti, V. Andersen, K. Lee, L. Pinsky, W. Atwell, R. Turner, and G. Badhwar (2004), Overview of the Martian radiation environment experiment, *Adv. Space Res.*, 33(12), 2204–2210.
- Zeitlin, C., et al. (2010), Mars Odyssey measurements of galactic cosmic rays and solar particles in Mars orbit, 2002–2008, *Space Weather*, 8, S00E06, doi:10.1029/2009SW000563.